

1 Temperature changes across the Paleocene-Eocene Thermal Maximum – a new  
2 high-resolution TEX<sub>86</sub> temperature record from the Eastern North Sea Basin

3 **Ella W. Stokke<sup>a,\*</sup>, Morgan T. Jones<sup>a</sup>, Jessica E. Tierney<sup>b</sup>, Henrik H. Svensen<sup>a</sup>, and Jessica H.**  
4 **Whiteside<sup>c</sup>**

5 <sup>a</sup> Centre for Earth Evolution and Dynamics (CEED), University of Oslo, PO Box 1028 Blindern,  
6 0315, Oslo, Norway. \*e.w.stokke@geo.uio.no

7 <sup>b</sup> The University of Arizona, Department of Geosciences, 1040 E 4<sup>th</sup> St Tucson, AZ 85721, USA.

8 <sup>c</sup> School of Ocean and Earth Science, National Oceanography Centre Southampton, University  
9 of Southampton, Southampton SO14 3ZH, United Kingdom.

## 10 Abstract

11 The Paleocene-Eocene Thermal Maximum (PETM; ~55.9 Ma) was a hyperthermal event  
12 associated with large carbon cycle perturbations, sustained global warming, and marine and  
13 terrestrial environmental changes. One possible trigger and/or source of the carbon release  
14 that initiated the PETM is the emplacement of the North Atlantic Igneous Province (NAIP). This  
15 study focuses on an expanded section of marine clays and diatomite on Fur Island in northern  
16 Denmark, where the entire PETM sequence have been identified by a negative ~4.5 ‰ δ<sup>13</sup>C<sub>TOC</sub>  
17 excursion. This remarkably well-preserved section also contains >180 interbedded ash layers  
18 sourced from the NAIP, making it an ideal site for investigating the correlations between large-  
19 scale volcanism and environmental changes. This study provides a new and complete high-  
20 resolution TEX<sub>86</sub>-derived sea-surface temperature (SST) reconstruction over the entire PETM  
21 and the post-PETM section (up to about 54.6 Ma). The palaeothermometry record indicates

22 an apparent short-lived cooling episode in the late Paleocene, followed by a pronounced  
23 temperature response to the PETM carbon cycle perturbations with a  $\sim 10$  °C SST increase  
24 during the PETM onset (up to  $\sim 33$  °C). Extreme SST temperatures fall shortly after PETM onset,  
25 and continue to decrease during the PETM body and recovery, down to anomalously cool SSTs  
26 post-PETM ( $\sim 11$ - $23$  °C). Both phases of potential cooling coincide with proxies of active NAIP  
27 volcanism, suggesting a causal connection, although several overprinting non-thermal factors  
28 complicate interpretations of the  $TEX_{86}$  values. Indices of effusive and explosive NAIP  
29 volcanism are largely absent from the Danish stratigraphy during the PETM body, though a re-  
30 emergence toward the end of the PETM suggest NAIP volcanism might have played a role in  
31 the PETM termination in the North Sea. This new SST record completes the previous  
32 fragmented view of climate changes at this globally important PETM site, and indicates large  
33 temperature variations in the North Sea during the earliest Eocene that are possibly linked to  
34 NAIP volcanism.

## 35 Keywords

36 PETM, North Atlantic Igneous Province, Palaeotemperatures,  $TEX_{86}$

## 37 1. Introduction

38 The Paleocene-Eocene Thermal Maximum (PETM) was an extreme hyperthermal event that  
39 punctuated the already greenhouse climate of the early Cenozoic (Zachos et al., 2010). The  
40 onset of the PETM was between 56.0 and 55.9 Ma (Charles et al., 2011; Westerhold et al.,  
41 2018; Zeebe and Lourens, 2019). It was associated with a global negative carbon isotopic  
42 excursion (CIE) of 3–5 ‰, attributed to the voluminous input of isotopically light carbon to the  
43 ocean and atmosphere (e.g. Zachos et al., 2010). This led to global ocean acidification,  
44 increased halocline stratification, and deep-sea anoxia (Babila et al., 2018; Kender et al., 2012;

45 Schoon et al., 2015). On land, temperature changes were accompanied by hydrological  
46 changes and mammalian biogeographic reorganisation (e.g. McInerney and Wing, 2011).  
47 There are several hyperthermal events in the Palaeogene, but the PETM is unique in terms of  
48 both the magnitude and duration of warming (Zachos et al., 2010). Several sources of  $^{12}\text{C}$ -rich  
49 carbon sources have been proposed for the PETM, including methane hydrates (Dickens et al.,  
50 1995), a bolide impact activating terrestrial carbon reservoirs (Schaller et al., 2016), and  
51 volcanic and thermogenic degassing from the North Atlantic Igneous Province (NAIP; Storey  
52 et al., 2007a; Svensen et al., 2004).

53 Existing PETM reconstructions of bottom-water temperature (BWT) and sea surface  
54 temperature (SST) show large variations in temperature increase, depending on depth,  
55 latitude, seawater chemistry, and the choice of proxy and calibration (Dunkley Jones et al.,  
56 2013; Frieling et al., 2017; Hollis et al., 2019). The severe ocean acidification and substantial  
57 deep-sea sediment dissolution during the PETM (Babila et al., 2018) puts severe limitations on  
58 applying carbonate-based temperature proxies such as Mg/Ca ratios and  $\delta^{18}\text{O}$  compositions  
59 (e.g. Dunkley Jones et al., 2013). In contrast, the organic SST proxy  $\text{TEX}_{86}$  is based on the  
60 relative distribution of glycerol dialkyl glycerol tetraethers (GDGT) membrane lipids of marine  
61 *Thaumarchaeota* (Schouten et al., 2002), and is therefore unaffected by carbonate  
62 dissolution. Unlike Mg/Ca and  $\delta^{18}\text{O}$ ,  $\text{TEX}_{86}$  is also insensitive to salinity and pH, and does not  
63 need to be corrected for ocean chemistry changes (Frieling et al., 2017; Hollis et al., 2019).  
64 This makes  $\text{TEX}_{86}$  ideal for investigating PETM temperatures, and has been applied to a  
65 number of PETM sections worldwide (Frieling et al., 2017; Schoon et al., 2015; Sluijs et al.,  
66 2006; 2011; Zachos et al., 2006).

67 The NAIP consists of extrusive and intrusive rocks around the modern Northeast Atlantic  
68 margins (Fig. 2). It was emplaced between 63-52 Ma, with the most voluminous activity  
69 occurring between 56-54 Ma during the opening of the North Atlantic (Storey et al., 2007b).  
70 Both the volcanic activity and contact metamorphism of organic-rich sediments are potentially  
71 major sources of carbon and other volatiles around the time of the PETM (Storey et al., 2007a;  
72 Svensen et al., 2004). The close proximity of the North Sea Basin to the NAIP makes this an  
73 ideal area to study climatic and volcanic proxies in the same section. NAIP-sourced tephras  
74 are numerous and widespread across the North Sea and in Denmark (e.g. King, 2016). A recent  
75 study also documented elevated Hg/TOC ratios in five continental shelf settings around the  
76 North Atlantic, interpreted as an indicator of elevated NAIP volcanic activity (Jones et al.,  
77 2019). An exceptionally well preserved and complete PETM section crops out on the island of  
78 Fur in northwest Denmark. It includes an expanded section of marine clays and interbedded  
79 ash layers, providing a unique opportunity to investigate a direct link between NAIP volcanism  
80 and PETM climatic changes.

81 Despite the clear advantages of studying the North Sea area, only one previous study has  
82 applied TEX<sub>86</sub> in this region, presenting records from two localities in Denmark (Fur Island and  
83 Store Bælt; Schoon et al., 2015; Fig. 1, 2). They documented a SST increase of 7–12 °C at the  
84 PETM onset, followed by an overall decrease back to pre-PETM values by the end of the CIE  
85 recovery. They also suggested a pre-PETM cooling in the Danish strata (Schoon et al., 2015),  
86 which is at odds with the pre-PETM warming identified in most PETM sites globally (Frieling et  
87 al., 2019). However, the existing record from Fur is sparse, with only 10 samples from the  
88 onset and recovery of the CIE. This preliminary study lacks high-resolution in key intervals and  
89 does not include data from the CIE body and post-PETM strata. Here, we present a new high-  
90 resolution record from Fur covering the entire PETM from the latest Paleocene, including post-

91 PETM sediments that have not been analysed before (Fig. 2). Constraining  
92 palaeotemperatures across significant climatic perturbations such as the PETM is crucial for  
93 understanding climate sensitivity and environmental change in the past, present, and future.  
94 By combining a detailed record of  $\delta^{13}\text{C}_{\text{TOC}}$  and  $\text{TEX}_{86}$  SST estimates in conjunction with volcanic  
95 proxies, we aim to evaluate the link between the palaeotemperature record and NAIP  
96 volcanism in the North Sea basin and expand the global temperature dataset during the PETM.

## 97 2. Materials and methods

### 98 2.1 Stratigraphy and sampling

#### 99 2.1.1 Stratigraphy

100 Fur is a small island (22 km<sup>2</sup>) in Limfjorden, Denmark (Fig. 2). During the latest Paleocene and  
101 earliest Eocene, thermal uplift around the NAIP led to the almost complete isolation of the  
102 North Sea Basin (Knox et al., 2010). Water depths around the study area were outer neritic,  
103 probably between 100–200 m (Knox et al., 2010; Schoon et al., 2015). The Paleocene-Eocene  
104 transition is marked at Fur by a shift in sedimentary facies from a condensed section of  
105 bioturbated Holmehus/Østerrende Fm. clay, into the dark, laminated clays of the Stolleklint  
106 Clay (Fig. 3, 4; Heilmann-Clausen et al., 1985; Schoon et al., 2015). A thin glauconitic silt unit  
107 (-24.61 to -24.55 m in Fig. 4, 5) marks the boundary, indicating a period of very slow  
108 sedimentation (Heilmann-Clausen et al., 1985). Although the boundary is poorly exposed at  
109 Fur, the glauconitic silt is likely underlain by an unconformity (~-24.6 m in Fig. 5; King, 2016;  
110 Schmitz et al., 2004). The PETM is identified just above the base of the Stolleklint Clay by a 4–  
111 8 ‰ negative CIE and appearance of the diagnostic dinoflagellate *Apectodinium augustum*  
112 (Jones et al., 2019; Schmitz et al., 2004; Schoon et al. 2015). The Stolleklint Clay grades upward  
113 into the ~60 m thick diatomite-rich Fur Fm. (Fig. 2b, 3, 4). More than 180 ash layers up to 20

114 cm thick are interbedded in the stratigraphy, with the majority (~140) found within the Fur  
115 Fm. (Fig. 3, 4). The volcanic ashes are grouped into a negative and positive ash series (Larsen  
116 et al., 2003), with additional ash layers (termed SK1, SK2, and SK3) within the base of the  
117 Stolleklint Clay (Fig. 4, 5). All of the ashes are sourced from NAIP explosive volcanism (Larsen  
118 et al., 2003), and distributed throughout the North Sea and Northern Europe (Larsen et al.,  
119 2003).

### 120 *2.1.2 Sampling*

121 This study focuses on the Stolleklint beach locality (Fig. 2a). Here, the PETM was identified just  
122 above the base of the Stolleklint Clay, while Ash -33 marks the end of the CIE body, and Ash -  
123 21 the final end of recovery (Jones et al., 2019). The sediments at Fur have experienced very  
124 little consolidation and lithification, leaving them soft and easy to sample. Recent  
125 glaciotectionic activity has created abundant small-scale folding and thrusting, although only  
126 one fault has been identified at Stolleklint, causing a doubling of Ash -33 (Fig. 4). High-  
127 resolution sampling was conducted throughout the section by combining samples from three  
128 different localities. The main locality is the Stolleklint beach (56°50'29"N, 8°59'33"E; Fig. 2a).  
129 Here, a 43 m long and 0.5 m deep trench was excavated (Fig. 2b) in order to reach the base of  
130 the Stolleklint Clay and the uppermost Holmehus/Østerrende Fm., which is otherwise poorly  
131 exposed. Jones et al. (2019) used careful trigonometry to estimate a local Stolleklint Clay  
132 thickness of  $24.4 \pm 2$  m (24.2 m excluding ash layers) from the base of Ash SK1 to the base of  
133 Ash -33. The lowermost part of the trench was sampled every cm from ~25 cm below to ~90  
134 cm above Ash SK1, recovering the entirety of the CIE onset. The remainder of the trench up  
135 to Ash -33 was sampled every 0.5 m (0.2–0.3 m estimated local thickness). Samples from the  
136 CIE recovery and lower post-PETM stratigraphy were collected from the cliff face at Stolleklint

137 (Fig. 2b) and from quarries near Fur Camping (FQ16 at 6°49'51''N, 8°58'45''E and PQ16 at  
138 56°49'48''N 8°59'07''E; Fig. 2a). Samples from Ash +1 upwards were collected from the quarry  
139 at Jenshøy (JH17; 56°50'05''N 9°00'31''E; Fig. 2a).

## 140 2.2 Analytical methods

### 141 2.2.1 Carbon isotopes

142 Analyses of total organic carbon (TOC) and stable carbon isotopes of bulk samples ( $\delta^{13}\text{C}_{\text{TOC}}$ )  
143 from Ash -11 and up were conducted at the Jahren Lab at the University of Oslo. Powdered  
144 samples were decalcified using 1M HCl, then oven-dried at 50 °C and re-homogenized. About  
145 8 mg of decalcified sample was sealed in tin capsules and loaded into a Costech Analytical  
146 Zero-Blank Autosampler. Organic  $\delta^{13}\text{C}_{\text{TOC}}$  measurements and TOC concentrations were  
147 analysed using a Thermo Fisher Scientific Flash Elemental Analyzer, coupled with a Thermo  
148 Fisher Scientific DeltaV Isotope Ratio Mass Spectrometer. Reproducibility of TOC and  $\delta^{13}\text{C}_{\text{TOC}}$   
149 was better than 0.01 wt% and 0.06 ‰, respectively. Previously published  $\delta^{13}\text{C}_{\text{TOC}}$  and TOC  
150 analyses from the base of the section up to Ash -13 from Jones et al. (2019) are included.

### 151 2.2.2 Molecular extraction and fractionation

152 Crushed samples (1 g) were extracted using a Thermo 350 Accelerated Solvent Extractor with  
153 the following program: preheat = 5 min; heat = 5 min; static = 5 min; pressure = 10.34 MPa;  
154 flush = 70 %, purge = 300 s.; cycles = 3; solvent = 9:1 dichloromethane:methanol. Solvent  
155 extracts were reduced to dry with a Genevac EZ-2 vacuum centrifuge. Total lipid extracts were  
156 quantified gravimetrically before column fractionation. Aliquots of the total lipid extracts were  
157 loaded onto small silica gel columns and fractions were eluted with hexane,  
158 hexane:dichloromethane (4:1), and dichloromethane:methanol (1:1) yielding the nonpolar,  
159 aromatic, and polar fractions, respectively.

160 2.2.3 GC- and LC-MS analysis

161 Aliphatic and aromatic fractions were desulphurised using copper beads, before being  
162 analysed for biomarker identification using a Thermo Trace 1310 gas chromatograph coupled  
163 to a Thermo TSQ8000 mass spectrometer at the National Oceanographic Centre,  
164 Southampton. The gas chromatograph used DB-5 column (30 m × 0.25 mm i.d, 0.25- $\mu$ m film  
165 thickness). The oven program was started at 40 °C (held for 2 min), increased at a rate of 6  
166 °C/min to 310 °C, and then held for 20 minutes. GC-MS analyses of the aliphatic and aromatic  
167 fractions generally yield low concentrations of biomarkers, with the *n*-alkanes and related  
168 compounds of  $m/z=57$  being the most abundant throughout. Compound identification of *n*-  
169 alkanes and pristane/phytane was made using mass spectra, library matches, and  
170 comparisons to known standards.

171 The polar fraction containing GDGTs was re-dissolved in hexane:isopropanol (99:1) and  
172 filtered with a 0.45 micron PTFE filter. The GDGTs were analysed on an Agilent 1260 Infinity  
173 HPLC coupled to an Agilent 6120 single quadrupole mass spectrometer at the University of  
174 Arizona, using two BEH HILIC silica columns (2.1 × 150 mm, 1.7  $\mu$ m; Waters) and the improved  
175 chromatographic methodology of Hopmans et al. (2016). We calculated peak areas using the  
176 MATLAB package software ORIGAmI (Fleming and Tierney, 2016).

177 2.2.4  $TEX_{86}$  values and calibration

178  $TEX_{86}$  values were calculated from isoprenoid GDGT (isoGDGT) peak areas according to  
179 Schouten et al. (2002), yielding values that are all within the calibration range in modern  
180 oceans (0.3 to 0.8; Fig. 4), suggesting that no extrapolation is required (Hollis et al., 2019).  
181 Several calibrations for estimating SSTs from  $TEX_{86}$  values have been developed, based on  
182 extensive modern global core-top datasets. The earliest calibration by Schouten et al. (2002)



183 used a linear relationship, which has since been shown to correlate poorly in temperatures <5  
184 °C and in some extreme settings such as the Red Sea (e.g. Kim et al., 2010). Other calibrations  
185 have been developed to circumvent this, such as the exponential calibration  $\text{TEX}_{86}^{\text{H}}$  (Kim et al.,  
186 2010), which excludes Red Sea data and temperatures below 10 °C. However, recent studies  
187 show that  $\text{TEX}_{86}^{\text{H}}$  has a statistical bias (regression dilution) that results in systematic  
188 underestimation of temperatures at high  $\text{TEX}_{86}$  values (Tierney and Tingley, 2014). Based on  
189 the recommendations of the DeepMIP model comparison project (Hollis et al., 2019), the use  
190 of  $\text{TEX}_{86}^{\text{H}}$  is no longer recommended for SST determinations in warm greenhouse climates. We  
191 refer readers to Hollis et al., (2019) for a full discussion of the limitations of  $\text{TEX}_{86}^{\text{H}}$  and  
192 recommendations for temperature estimates in the PETM and early Eocene intervals.

193 Following DeepMIP recommendations, we apply the Bayesian regression model BAYSPAR  
194 (Tierney and Tingley, 2014) to convert  $\text{TEX}_{86}$  values to SSTs. The linear BAYSPAR calibration  
195 varies its regression terms spatially, taking into account the regional differences in the  
196 relationship between SST and  $\text{TEX}_{86}$  that are observed today (Tierney and Tingley, 2014).  
197 BAYSPAR also includes modern Red Sea data, which is likely a strength as Red Sea-type  
198 distributions are commonly observed in PETM and early Eocene sites (Hollis et al., 2019).  
199 However, for deep-time applications, BAYSPAR is run in analogue mode, which does not use  
200 regionally-specific calibration parameters. Rather, analogue mode uses all regression  
201 parameters associated with  $\text{TEX}_{86}$  values within a specified threshold of the data, regardless  
202 of location. We applied BAYSPAR to infer SST with the following settings: prior mean = 20,  
203 prior standard deviation = 10,  $\text{TEX}_{86}$  tolerance = 0.15, number of iterations = 2500. As  $\text{TEX}_{86}^{\text{H}}$   
204 has been applied to other PETM sites, the  $\text{TEX}_{86}^{\text{H}}$  calibration can be found in the  
205 Supplementary data for comparative use.

### 206 2.2.5 Other biomarker indices

207 There are several caveats and overprinting factors that can potentially bias  $\text{TEX}_{86}$  values,  
208 particularly through the addition of isoGDGTs that are not produced by Thaumarchaeota in  
209 the upper water column. Several methods are applied to assess the potential bias of  $\text{TEX}_{86}$   
210 values. The Branched and Isoprenoid Tetraether (BIT) index measures the relative input of  
211 terrestrially derived branched GDGTs (brGDGT) and the marine-derived crenarchaeol. BIT was  
212 calculated following Hopmans et al. (2004). BIT values above 0.4 may indicate that  $\text{TEX}_{86}$   
213 temperatures are compromised by terrestrially-derived isoGDGTs (Weijers et al., 2006).  
214 However, there is no universal cut-off for BIT values as BIT does not straightforwardly relate  
215 to terrestrial organic matter (OM) fluxes and brGDGTs can also be produced *in situ* in marine  
216 environments (e.g. Peterse et al., 2009).

217 The Methane Index (MI) assess the potential influence of methanotrophic and methanogenic  
218 GDGT producers, which can bias  $\text{TEX}_{86}$  values (Zhang et al., 2011). MI values  $>0.5$  characterize  
219 sedimentary conditions with a substantial methanogenic influence, typically in anoxic basins  
220 or near methane seeps (Zhang et al., 2011). Methanogenic archaea can also synthesize GDGT-  
221 0 (Blaga et al., 2009). The ratio GDGT-0/Crenarchaeol has been suggested as an indicator of  
222 methanogenesis on the isoGDGT population, with a substantial contribution indicated by  
223 values  $>2$  (Blaga et al., 2009). The delta-ring index ( $\Delta\text{RI}$ ; Zhang et al., 2016) detects whether  
224 the isoGDGT distributions differ from the surface calibration dataset. It can indicate if other  
225 factors than temperature is controlling the GDGT distribution, often detecting anything that  
226 would otherwise be flagged by BIT and MI.  $\Delta\text{RI}$  is calculated by comparing the temperature  
227 dependent Ring Index (RI) and  $\text{TEX}_{86}$  to the modern global  $\text{TEX}_{86}$ -RI relationship, with an upper  
228 limit of  $|0.3|$  (95 % confidence interval of the modern regression).  $\text{TEX}_{86}$  derived SSTs where

229 BIT values are  $>0.4$  are shown as open circles (Fig. 4, 5). All samples where  $\Delta RI$  exceeds  $|0.3|$   
230 also have  $BIT > 0.4$ , and have been marked red in Fig. 3 and 4. All marked samples should be  
231 interpreted with some care.

232 Additional environmental constraints are indicated by biomarker proxies from the aliphatic  
233 fraction analysed with GC-MS. The Terrigenous Aquatic Ratio (TAR; Peters et al., 2005) is a  
234 proxy of potential terrigenous input relative to marine. It is defined as the ratio of the primarily  
235 land-plant derived long-chain *n*-alkanes  $nC_{27}$ ,  $nC_{29}$  and  $nC_{31}$ , over the short-chain *n*-alkanes  
236  $nC_{15}$ ,  $nC_{17}$  and  $nC_{19}$  mainly derived from marine algae. Pristane and phytane are derived from  
237 the phytol side-chains of chlorophyll in algae and bacteria. These can be used as a proxy for  
238 both source region and redox conditions. Reducing conditions promote the reduction of  
239 phytol to phytane, while oxic conditions leads to oxidation of phytol to pristane (Peters et al.,  
240 2005).

### 241 3. Results and Discussion

#### 242 3.1 Shape and duration of the PETM at Fur

243 The Fur stratigraphy is an outstanding locality, comprising an uninterrupted PETM section of  
244 well-preserved marine clays. GC-MS measurements show that the *n*-alkanes have a constant  
245 high odd-over-even preference (OEP; Supplement), with  $OEP > 1$  throughout indicating that  
246 the whole sequence is thermally immature and well suited for organic geochemical analyses  
247 (Peters et al., 2005).

248 The late Paleocene Holmehus/Østerrende Fm. show stable  $\delta^{13}C_{TOC}$  values around  $-26 \text{ ‰}$ , and  
249 TOC concentrations of  $\sim 0.5 \text{ wt\%}$  (Fig. 4, 5). The C25r-C25n boundary ( $\sim 57.7 \text{ Ma}$ ; Ogg et al.,  
250 2012) marks the top of the Holmehus Fm., but the duration of the overlying unconformity is  
251 undefined as it is unclear how much of the overlying Østerrende Fm. is present at Fur (Fig. 3;

252 King, 2016). The  $\delta^{13}\text{C}_{\text{TOC}}$  values in the overlying glauconitic unit remain stable at  $\sim -26$  ‰ while  
253 TOC values drop to about 0.3 wt%. Neither the age nor duration of the glauconitic silt is well  
254 constrained, although it is most likely a part of the basal section of the Stolleklint clay, similar  
255 to that described at Ølst  $\sim 80$  km to the southeast (Fig. 2; King, 2016; Schmitz et al., 2004). The  
256 glauconitic layer is  $\sim 5$  m thick at the Store Bælt section but only  $\sim 5$  cm thick at Ølst and  
257 Stolleklint (Fig. 2; Schmitz et al., 2004; Schoon et al., 2015), suggesting that it is highly  
258 condensed. An interstitial clay (between ashes SK1 and SK2) with  $\sim 0.4$  wt% TOC is found above  
259 the glauconitic silt prior to the PETM onset (Fig. 4, 5).

260 The PETM onset is defined by a sharp CIE of  $\sim -4.5$  ‰ (from  $-26.5$  to  $-31$  ‰) immediately above  
261 Ash SK2, which is larger than average bulk marine OM records (McInerney and Wing, 2011).  
262 The CIE onset at Fur was concordant with the sudden dominance of the subtropical  
263 dinoflagellate *Apectodinium augustum* (Heilmann-Clausen et al., 1985; King, 2016). A  
264 pronounced increase in TOC from 0.45 to 1.5 wt% and a shift from bioturbated to laminated  
265 clays occur  $\sim 2$  cm above the CIE onset (Fig. 4, 5), suggesting a shift to anoxic conditions. TOC  
266 concentrations remain relatively stable for the first half of the CIE body, before increasing up  
267 to 3.9 wt% in the upper half (Fig. 4). This large increase in TOC is followed by a shift from dark  
268 laminated clays to massive, black clays with abundant pyrite suggesting a highly anoxic  
269 environment. Just above Ash -33 at the start of the CIE recovery, TOC concentrations drop to  
270  $<1$  wt%.

271 The CIE body is defined by an extended interval ( $\sim 24$  m) of sustained stable negative  $\delta^{13}\text{C}_{\text{TOC}}$   
272 values (Fig. 4). In contrast, the recovery phase is relatively sharp, starting at Ash -33 and  
273 returning to pre-PETM values by Ash -21 ( $\sim 4.5$  m thick; Fig. 4). The small thrust fault that cuts  
274 across Ash -33 in parts of the Stolleklint beach section likely leads to some uncertainty about

275 the exact shape and duration of the  $\delta^{13}\text{C}_{\text{TOC}}$  curve during the shift from CIE body to recovery  
276 (Fig. 4). The unusually thick CIE body at Fur most likely reflects a large increase in  
277 sedimentation rates during the PETM CIE that wanes again during the recovery. Jones et al.  
278 (2019) estimated a 24.2 m ash-free thickness of the CIE body at Stollekint. If a 100 kyr for the  
279 PETM body (van de Meulen et al., 2020), the sediment accumulation rate for the Stollekint  
280 Clay is about 24 cm/kyr (24.2 m/100 kyr). Considering the condensed and bioturbated nature  
281 of the underlying glauconitic silt, this indicates a considerable increase in sedimentation rate.  
282 The increasingly diatomite-dominated lithology suggests a decreasing sedimentation rate  
283 during the CIE recovery and post-PETM sections.

284 The post-PETM period section is characterised by  $\delta^{13}\text{C}_{\text{TOC}}$  values that fluctuate between -26  
285 and -28 ‰ (Fig. 4), typical for bulk marine OM records at this time (McInerney and Wing,  
286 2011). The lower, laminated part of the post-PETM section (~+4 to +20 m in Fig. 4) is composed  
287 of a relatively clayey diatomite showing variable TOC concentrations (0.5 to 3.2 wt%). In  
288 contrast, the uppermost ~20 m of the stratigraphy comprised almost entirely of diatomite has  
289 stable low concentrations around 0.5 wt% TOC. The age control on the post-PETM Fur Fm. is  
290 limited as only the post-PETM Ash -17 is so far radioisotopically dated (Storey et al., 2007a),  
291 with a recalibrated Ar-Ar age of  $55.6 \pm 0.12$  Ma (Jones et al., 2019). Westerhold et al. (2009)  
292 estimated a 200 kyr duration between Ash -17 and +19, placing Ash +19 at about 55.4 Ma (Fig.  
293 6) and a total 300 kyr duration of the positive ash series. Stratigraphic correlations with the  
294 lower Balder Fm. places the top of the Fur Fm. as  $\geq 54.6$  Ma (King, 2016), prior to the onset of  
295 the Eocene Thermal Maximum 2 (ETM 2; Fig. 3).

## 296 3.2 Constraining PETM temperature changes

### 297 3.2.1 Apparent late Paleocene cooling

298 The late Paleocene interval comprises the lowermost ~65 cm of the stratigraphy (Fig. 4, 5).  
299 The Holmehus/Østerrende Fm. is characterized by relatively stable SSTs around ~23 °C (Fig.  
300 5). BAYSPAR calibrated SSTs drop down to a minimum of  $14.5 \pm 3 [1\sigma]$  °C ~2 cm below Ash SK1  
301 (Fig. 5), corresponding to a SST drop of ~8 °C (Fig. 5). This corroborates the preliminary findings  
302 of Schoon et al. (2015), who found evidence of a pre-PETM cooling event from two samples  
303 at Stolleklint. However, the age of the late Paleocene strata below SK2 is poorly constrained.  
304 While there is no compelling evidence for hiatuses within the sediments above the glauconitic  
305 unit, considering the bioturbation in these sediments we cannot rule one out either. The  
306 timing of the cooling is therefore late Paleocene (<57.7 Ma; King, 2016), although it could be  
307 just prior to the onset of the PETM.

308 This apparent cooling interval can be divided in two, with the lower part found in the  
309 glauconitic silt below Ash SK1 and the upper in the interstitial clay between Ashes SK1 and  
310 SK2. The entire cooling interval is characterized by low abundances of the Crenarchaeol isomer  
311 (Cren'; Supplement), suggesting a slightly different Thaumarchaeota population in this  
312 interval. The cooling onset coincides with increases in several overprinting signals that can  
313 bias TEX<sub>86</sub> values (Fig. 5; Supplement). Firstly,  $\Delta RI$  increases sharply and exceeds threshold  
314 values of |0.3| at the start of the cooling, suggesting non-thermal factors likely control the  
315 GDGT distribution (Zhang et al., 2016). Both MI and GDGT-0/Crenarchaeol are elevated in the  
316 same interval (MI up to 0.3, GDGT-0/Cren up to 1.9; Fig. 5; Supplement) suggesting potential  
317 methanogenic influence (Blaga et al., 2009; Zhang et al., 2011). An abrupt increase in TAR  
318 (from 0.7 to 4.3) and BIT (up to 0.8) in the base of the glauconitic silt suggests a large increase

319 in terrestrial input influencing TEX<sub>86</sub> values (Fig. 5; Peters et al., 2005; Weijers et al., 2006).  
320 Preferential degradation of isoGDGTs due to oxic degradation could also have an influence,  
321 potentially resulting in increased BIT values and lower absolute temperatures (Hopmans et  
322 al., 2004). Bioturbation, low TOC concentration, and pristane/phytane partly >1 indicate  
323 relatively oxygenated conditions below Ash SK1 (Fig. 5).

324 Low TEX<sub>86</sub> values and inferred cooling continues in the upper part between Ashes SK1 and SK2.  
325 While the upper part is slightly affected by elevated BIT values (from 0.27 to 0.43; Fig. 5),  $\Delta RI$   
326 decreases below threshold values and there is no compelling evidence of methanogenic  
327 influence (Fig. 5; Supplement). Despite the elevated BIT values, the low  $\Delta RI$  suggests that the  
328 TEX<sub>86</sub> values are likely to be robust. Schoon et al. (2015) observed a similar cooling in mean  
329 annual air temperatures (MAAT) from this interval, reconstructed from soil-derived brGDGTs.  
330 While brGDGTs may be produced *in-situ* (e.g. Peterse et al., 2009) and offset MAAT estimates,  
331 a separate corroborating proxy could support the presence of a cooling event before the CIE  
332 onset. Inglis et al. (2019) also describe a terrestrial cooling during the PETM onset in England,  
333 although they argue strongly that this is due to caveats with the brGDGT palaeothermometer.  
334 The presence of a cooling before the CIE is at odds with most other PETM sections, where  
335 temperatures are either stable (e.g. Sluijs et al., 2006) or even show a pre-CIE warming  
336 (Frieling et al., 2019). However, it is possible that the absence of any pre-PETM warming at  
337 Fur could be due to a regional cooling event affecting the North Sea. The interval between  
338 Ashes SK1 and SK2 is unlikely to be adversely affected by TEX<sub>86</sub> bias, suggesting that the cooling  
339 observed is a real feature. However, the numerous overprinting factors and  
340 missing/condensed stratigraphy in the lower glauconitic silt indicates that more work is  
341 needed to constrain the likelihood and duration for such a cooling event.

342 3.2.2 PETM warming and recovery

343 The PETM onset, body and recovery show consistently low  $\Delta RI$ , MI, and BIT indices, indicating  
344  $TEX_{86}$  values are likely unbiased. While BIT values are consistently low ( $<1$ ) throughout the CIE  
345 body, changing TAR values indicating variable input of long-chain *n*-alkanes from terrigenous  
346 sources during the PETM (Fig. 4). The  $\sim -4.5$  ‰ CIE marking the PETM onset at Fur is followed  
347 closely by a SST increase to about 30 °C (Fig. 5). Maximum PETM SSTs of  $33.3 \pm 4$  [ $1\sigma$ ] °C is  
348 reached only  $\sim 1.8$  m above the CIE onset (Fig. 4, 5), suggesting a relatively rapid temperature  
349 response to carbon release. The temperature increase at Fur represents a minimum estimate  
350 of 10 °C warming from late Paleocene values (Fig. 4, 5). The  $TEX_{86}^H$  calibration is within the  $1\sigma$   
351 calibration error of BAYSPAR, and shows the same relative trend with lower maximum and  
352 higher minimum SST's resulting in a minimum 7 °C PETM warming (Supplement). A 7–10 °C  
353 SST warming is at the upper end of previous estimates for the PETM (Dunkley Jones et al.,  
354 2013; Frieling et al., 2017), although it is important to note that  $TEX_{86}$  typically yield slightly  
355 higher SSTs than other proxies (e.g. Inglis et al., 2020). The warming agrees relatively well with  
356 other mid-latitude shelf settings (Frieling et al., 2014; Zachos et al., 2006) and the Southern  
357 Ocean (Sluijs et al., 2011), but is higher than those observed in the Tropics (Frieling et al.,  
358 2017), the Arctic (Sluijs et al., 2006), and deeper mid-latitude settings (e.g. Bay of Biscay;  
359 Bornemann et al., 2014). However, spatial variability of warming and high latitude  
360 amplification have been described both from modelling and proxy studies during the PETM  
361 (Dunkley Jones et al., 2013; Frieling et al., 2017). The estimated temperature increase and  
362 estimated maximum PETM SSTs also agrees well with recently modelled Global Mean Surface  
363 Temperature for the PETM of 33 °C and a temperature increase of 4–9 °C from latest  
364 Paleocene (Inglis et al., 2020).



365 The negative  $\delta^{13}\text{C}_{\text{TOC}}$  values are near constant throughout the PETM body phase until Ash -33  
366 (Fig. 4), indicating continued input of depleted carbon and little change to the carbon isotope  
367 composition of the surface carbon reservoir. However, after reaching maximum SSTs shortly  
368 after the onset, temperatures decline throughout the remainder of the PETM and return to  
369 late Paleocene values by the end of the CIE recovery (Fig. 4). This suggests that negative  
370 feedback mechanisms lowering temperatures were active during the PETM, such as increased  
371 silicate weathering and OM burial, removing  $\text{CO}_2$  from the atmosphere (McInerney and Wing,  
372 2011). Sedimentation rates increase at Fur and globally during the PETM, reflecting enhanced  
373 weathering in response to a stronger hydrological cycle (Kender et al., 2012). Increased  
374 productivity and OM burial in shelf settings has been demonstrated globally (Ma et al., 2014),  
375 and likely had an important role in atmospheric carbon drawdown (e.g. Gutjahr et al., 2017).  
376 John et al. (2008) suggested that due to drastically increased sedimentation rates and  
377 productivity during the PETM, mid-latitude shelves became highly efficient sinks for organic  
378 carbon burial. The substantial increase in sedimentation rate during the PETM and in OM  
379 burial in the upper half of the CIE body at Fur (Fig. 4), corroborates the important role for  
380 shelves in carbon drawdown and the final PETM CIE recovery.

### 381 3.3 Post-PETM temperature variations

382 Temperatures drop during the CIE recovery to a minimum of  $15 \pm 3 [1\sigma]$  °C, 1 m above Ash -  
383 21a. An initial increase in SSTs up to  $23.6 \pm 3.3 [1\sigma]$  °C (+15 m in Fig. 4) is followed by varying  
384 SSTs (11–23 °C) during the post-PETM (Fig. 4). While the lower 15 m have low  $\Delta\text{RI}$ , MI, and BIT  
385 indices indicating relatively robust  $\text{TEX}_{86}$  values, the upper 25 m are characterized by a number  
386 of overprinting factors.  $\Delta\text{RI}$  values are high and exceeding  $|0.3|$  in several samples, suggesting  
387 non-thermal factors are controlling isoGDGT distribution (Zhang et al., 2016). High BIT ratios

388 prevail, with values  $>0.4$  for all samples above +21 m height (Fig. 4). This may reflect inclusion  
389 of soil derived branched GDGTs (Hopmans et al., 2004; Weijers et al., 2006), although low TAR  
390 values suggest this section is dominated by marine-sourced short-chain *n*-alkanes (Fig. 4;  
391 Peters et al., 2005). Concentrations of brGDGTs are also low and sometimes below detection  
392 limit in the post-PETM section (Fig. 4; Supplement), which may compromise BIT values.  
393 Alternatively, the high BIT ratios could reflect preferential oxic degradation of marine  
394 isoGDGTs. This is supported by the low TOC concentrations and high pristane/phytane ratios  
395 (Fig. 4). While MI values are all  $<0.3$  (Fig. 4, 5), the GDGT-0/Crenarchaeol ratio is relatively high  
396 in several samples post-PETM ( $>2$  at  $\sim+35$  m height; Supplement), suggesting a potential for  
397 limited methanogenesis (Blaga et al., 2009).

398 Although there are many possible factors affecting  $\text{TEX}_{86}$  values, the general trend of lower  
399 post-PETM temperatures is likely to be a real feature. The Fur Fm. was deposited during a  $\sim 1$   
400 Myr period before 54.6 Ma (King, 2016), thus predating ETM2 and the Early Eocene Climatic  
401 Optimum (Fig. 3, 6). Global temperatures show a general cooling after the PETM (Cramwinckel  
402 et al., 2019; Frieling et al., 2017; Inglis et al., 2020), although the post-PETM SSTs at Fur seem  
403 anomalously low compared to similar mid-latitude sites (Frieling et al., 2014; Bornemann et  
404 al., 2014). This is particularly true for the lowest SSTs recorded just above the CIE recovery ( $15$   
405  $\pm 3 [1\sigma]$  °C at +5.5 m in Fig. 4), where potential  $\text{TEX}_{86}$  bias is least. A diversity reduction in plant  
406 communities in the Shetland basin has also been inferred to indicate lowered surface  
407 temperature in the period between the PETM and the ETM2 (Jolley and Widdowson, 2005). It  
408 is therefore possible that regional conditions led to enhanced cooling in the Danish region and  
409 possible larger parts of the Northeast Atlantic.

### 410 3.4 The role of North Atlantic Igneous Province volcanism

411 The NAIP is known to have been particularly active across the PETM. The dominant mode of  
412 eruption was effusive, building up huge continental flood basalts in Greenland and the Faroe  
413 Islands (Fig. 2). Constraints on timing and duration of the East Greenland lavas suggest that a  
414 5–6 km thick lava pile was emplaced between 56.0 and 55.6 Ma (Jones et al., 2019; Larsen and  
415 Tegner, 2006). However, there is currently no data on whether these eruptions were  
416 continuous, pulsed, or constrained to a much shorter time window. This has significant  
417 implications for the NAIP as a potential climate forcing. The main climatic impact of large  
418 eruptions is cooling, caused by sulphuric acid aerosols in the atmosphere increasing the  
419 planetary albedo (Robock, 2000). Atmospheric residence times for sulphur depend on  
420 whether it reaches the stratosphere (1-3 years), or if it is released to the troposphere (weeks).  
421 This means that dominantly tropospheric emissions would result in a more regionally  
422 constrained cooling. A historic example is the 1783-84 eruption of Laki (Iceland) that caused a  
423 2-3 years of cooling largely constrained to the northern hemisphere (Thordarson and Self,  
424 2003). However, the limited residence time of sulphur in the atmosphere restricts the duration  
425 of climatic impact to essentially syn-eruptive (Jones et al., 2016), which means transient  
426 cooling events from rapid explosive eruptions would not be preserved in the  
427 palaeotemperature record. Modelling has shown that the global climate can recover from  
428 perturbations during large effusive eruptions (4-6 °C cooling) within 50 years of the eruption  
429 end (Schmidt et al., 2016). Therefore, the only potential method of preserving volcanic cooling  
430 in sedimentary sequences would be near-continuous eruptions over several centuries. The  
431 duration and repose times of periods of quiescence between eruptions are therefore a  
432 particularly important factor.

433 The hundreds of ash layers preserved in North Sea sediments indicate widespread explosive  
434 volcanism associated with the NAIP (Larsen et al., 2003). However, explosive eruptions are  
435 typically a minor volumetric component of LIPs. The unusual prevalence of basaltic tephra  
436 suggests that the explosiveness of eruptions was enhanced by magma-seawater interaction  
437 as Greenland and Eurasia broke apart (Larsen et al., 2003). Therefore, the increase in ash  
438 layers in the upper parts of the Fur stratigraphy likely reflect a change in eruptive style, rather  
439 than an increase in total volcanism. The positive ash series follows a period of long-lasting  
440 effusive flood basalt eruptions, which typically do not produce large amounts of ash, but do  
441 provide a constant supply of sulphur and other volcanic gases. While the volcanic ash layers  
442 mainly reflect periods of explosive volcanic activity, Hg/TOC anomalies indicate both the  
443 explosive and effusive activity.

444 Evidence from the Danish stratigraphy suggests at least four episodes of enhanced NAIP  
445 volcanism (Fig. 6). The first period occurs in the late Paleocene prior to the PETM onset, and  
446 is indicated by Hg/TOC anomalies (Jones et al., 2019) and the deposition of Ashes SK1 and SK2  
447 (Fig. 5, 6). This period of prolonged and enhanced volcanic activity prior to the PETM onset  
448 coincides with the  $TEX_{86}$  derived apparent cooling (Fig. 5, 6). Active NAIP volcanism is  
449 corroborated in the pre-PETM strata in Svalbard, where large Hg/TOC anomalies have been  
450 documented (Jones et al., 2019), together with low  $^{187}Os/^{188}Os$  values suggesting weathering  
451 of substantial volumes of basaltic material (Wieczorek et al., 2013). The North Sea Basin is  
452 ideally placed to record potential volcanic cooling due to its close proximity to the NAIP and  
453 being downwind of the easterly polar jet stream. If effusive volcanism led to largely  
454 tropospheric degassing, then the surface cooling would be most prominent in the North Sea  
455 area and potentially absent from distal records, particularly in the tropics and southern  
456 hemisphere.

457 It is important to note that volcanic activity is one of several factors that could potentially  
458 explain the available SST proxy data. Thermal uplift from the NAIP led to the isolation of the  
459 North Sea during the latest Paleocene and earliest Eocene (Knox et al., 2010), which would  
460 have changed the oceanographic conditions. This could have affected the degree of mixing  
461 and therefore heat transport in the North Sea basin, potentially leading to slightly cooler SST  
462 conditions in the late Paleocene. A bolide impact has been identified at the Paleocene-Eocene  
463 transition that may have cooled surface temperatures through impact ejecta (Schaller et al.,  
464 2016). However, no indices of such an event have been found in Denmark (Schmitz et al.,  
465 2004) and the impact is placed at the CIE onset (Schaller et al., 2016), thereby post-dating the  
466 apparent cooling. If the observed cooling is a true indication of palaeotemperatures, then the  
467 most plausible explanation is that NAIP volcanism led to a regional cooling in the late  
468 Paleocene before the CIE onset in the interval between Ashes SK1 and SK2 (Fig. 5). However,  
469 temperature reconstructions from other areas proximal to the NAIP are sparse. More work is  
470 needed around the northeast Atlantic margins to confirm whether the apparent cooling is  
471 real, its exact timing and duration, and to constrain the potential regional distribution of  
472 cooling.

473 There is no compelling evidence for enhanced volcanism during most of the PETM body in the  
474 Danish strata (Fig. 6). This is noteworthy as the ~100 kyr CIE body interval occurs during the  
475 ~400 kyr (56.0–55.6 Ma) interval known for elevated NAIP volcanism (Gutjahr et al., 2017;  
476 Larsen and Tegner, 2006). This includes the important phase of sill emplacement and  
477 thermogenic degassing through hydrothermal vent complexes (Svensen et al., 2004; Frieling  
478 et al., 2016). The available proxies from Fur do not shed light on the timing nor duration of the  
479 thermogenic degassing phase of the NAIP. The cooling during the PETM recovery is coincident  
480 with the re-emergence of thick ash layers and Hg/TOC anomalies (Fig. 6). Temperatures

481 decrease >10 °C during the CIE recovery (Fig. 4), and the abundance of volcanic proxies in the  
482 Danish strata toward the end of the CIE body and into the CIE recovery suggests that the  
483 effects of volcanism (e.g. sulphate aerosols, weathering) may also have contributed to the  
484 cessation of hyperthermal conditions. The >140 ash layers present in post-PETM strata  
485 indicate intense and long-lasting explosive volcanism (Fig. 4, 6). This periods of enhanced  
486 volcanic activity coincide with the TEX<sub>86</sub> derived cool SSTs (Fig. 4, 6). A similar cooling is  
487 suggested within the exceptionally ash rich contemporaneous Balder Fm. (Fig. 3) of the  
488 Shetland basin (Jolley and Widdowson, 2005). It is possible that the period of exceptionally  
489 explosive volcanic activity following the PETM (Fig. 6) led to a period of regionally cooler  
490 temperatures in the North Sea and Northeast Atlantic region.

## 491 5. Conclusions

492 A ~-4.5 ‰ change in  $\delta^{13}\text{C}_{\text{TOC}}$  defines the PETM onset in an expanded section at Fur Island,  
493 Denmark. The CIE onset is accompanied by a marked lithological transition from bioturbated  
494 to laminated clays and a dramatic increase in both sedimentation rate and OM content. The  
495 late Paleocene section shows an apparent SST cooling of up to 8 °C, based on the TEX<sub>86</sub> proxy.  
496 While the large potential for TEX<sub>86</sub> bias during the first stage make validity of this cooling  
497 episode somewhat speculative, the potential TEX<sub>86</sub> bias decrease substantially suggesting the  
498 latest stage may represent a genuine cooling episode. This latest robust stage of apparent  
499 cooling coincides with deposition of two major ash layers (SK1 and SK2) and significant Hg/TOC  
500 anomalies, suggesting that regional cooling from voluminous volcanism may be the cause of  
501 temporally depressed SSTs in the North Sea during the late Paleocene.

502 TEX<sub>86</sub>-derived SSTs yield a minimum temperature increase of ~10 °C across the CIE onset,  
503 depending on the calibration method used. This temperature increase is within previous

504 estimates for the PETM, though at the upper end. Maximum SST is reached relatively shortly  
505 after the CIE onset, followed by a shift to gradually declining temperatures. There is evidence  
506 for negative feedbacks to warming, such as silicate weathering and organic matter burial,  
507 occurring during the stable body phase of the PETM CIE. SSTs decreased substantially,  
508 reaching anomalously low temperatures by the end of the CIE recovery. A re-emergence of  
509 volcanic proxies during the end of the CIE body and the CIE recovery, suggest the effects of  
510 volcanism may have contributed to the cessation of hyperthermal conditions. During the post-  
511 PETM interval, TEX<sub>86</sub>-derived SSTs are variable and partly anomalously low (11–23 °C). While  
512 overprinting factors could affect TEX<sub>86</sub>-derived SSTs in parts of the stratigraphy, the effect of  
513 persistent explosive volcanic activity during this period is likely to have had some effect on  
514 SSTs in the North Sea region.

#### 515 Acknowledgments

516 We thank reviewer Dr. Peter Bijl, the anonymous reviewer, and editor Dr. Laura Robinson, for  
517 their very thorough and constructive comments. Prof. Emeritus Claus Heilmann-Clausen, Dr.  
518 Joost Frieling is sincerely thanked for good and helpful discussions. P. Sargent Bray, Bo Schultz,  
519 Dr. Sverre Planke, Prof. Christian Tegner, and Dr. Valentin Zuchuat are all warmly thanked for  
520 their assistance. This project was supported by the Research Council of Norway's funding  
521 schemes "Unge Forskertallenter" project number 263000 (project Ashlantic) and "Centres of  
522 Excellence" project number 223272, and their funding to the Norwegian Research School  
523 DEEP with project number 249040/F60. J. Whiteside is thankful to support from an Annual  
524 Adventures in Research grant. J. Tierney acknowledges support from the David and Lucile  
525 Packard Foundation and the Heising-Simons Foundation Grant #2016-015.

526 References

- 527 Babila, T. L., Penman, D. E., Hönisch, B., Kelly, D. C., Bralower, T. J., Rosenthal, Y., & Zachos, J.  
528 C. (2018). Capturing the global signature of surface ocean acidification during the Palaeocene–  
529 Eocene Thermal Maximum. *Philosophical Transactions of the Royal Society A: Mathematical,*  
530 *Physical and Engineering Sciences*, 376(2130), 20170072.
- 531 Blaga, C. I., Reichert, G. J., Heiri, O., & Damsté, J. S. S. (2009). Tetraether membrane lipid  
532 distributions in water-column particulate matter and sediments: a study of 47 European lakes  
533 along a north–south transect. *Journal of Paleolimnology*, 41(3), 523-540.
- 534 Bornemann, A., Norris, R. D., Lyman, J. A., D'haenens, S., Groeneveld, J., Röhl, U., ... & Speijer,  
535 R. P. (2014). Persistent environmental change after the Paleocene–Eocene Thermal Maximum  
536 in the eastern North Atlantic. *Earth and Planetary Science Letters*, 394, 70-81.
- 537 Charles, A. J., Condon, D. J., Harding, I. C., Pälike, H., Marshall, J. E., Cui, Y., ... & Croudace, I.  
538 W. (2011). Constraints on the numerical age of the Paleocene-Eocene boundary.  
539 *Geochemistry, Geophysics, Geosystems*, 12(6).
- 540 Cramer, B. S., Toggweiler, J. R., Wright, J. D., Katz, M. E., & Miller, K. G. (2009). Ocean  
541 overturning since the Late Cretaceous: Inferences from a new benthic foraminiferal isotope  
542 compilation. *Paleoceanography*, 24(4).
- 543 Cramwinckel, M. J., Huber, M., Kocken, I. J., Agnini, C., Bijl, P. K., Bohaty, S. M., ... & Peterse,  
544 F. (2018). Synchronous tropical and polar temperature evolution in the Eocene. *Nature*,  
545 559(7714), 382-386.



546 Dickens, G. R., O'Neil, J. R., Rea, D. K., & Owen, R. M. (1995). Dissociation of oceanic methane  
547 hydrate as a cause of the carbon isotope excursion at the end of the Paleocene.  
548 *Paleoceanography and Paleoclimatology*, 10(6), 965-971.

549 Dunkley Jones, T., Lunt, D. J., Schmidt, D. N., Ridgwell, A., Sluijs, A., Valdes, P. J., & Maslin, M.  
550 (2013). Climate model and proxy data constraints on ocean warming across the Paleocene–  
551 Eocene Thermal Maximum. *Earth-Science Reviews*, 125, 123-145.

552 Fleming, L. E., & Tierney, J. E. (2016). An automated method for the determination of the  
553 TEX86 and U37K' paleotemperature indices. *Organic geochemistry*, 92, 84-91.

554 Frieling, J., Iakovleva, A. I., Reichart, G. J., Aleksandrova, G. N., Gribidenko, Z. N., Schouten, S.,  
555 & Sluijs, A. (2014). Paleocene–Eocene warming and biotic response in the epicontinental West  
556 Siberian Sea. *Geology*, 42(9), 767-770.

557 Frieling, J., Svensen, H. H., Planke, S., Cramwinckel, M. J., Selnes, H., & Sluijs, A. (2016).  
558 Thermogenic methane release as a cause for the long duration of the PETM. *Proceedings of*  
559 *the National Academy of Sciences*, 113(43), 12059-12064.

560 Frieling, J., Gebhardt, H., Huber, M., Adekeye, O. A., Akande, S. O., Reichart, G. J., ... & Sluijs,  
561 A. (2017). Extreme warmth and heat-stressed plankton in the tropics during the Paleocene–  
562 Eocene Thermal Maximum. *Science advances*, 3(3), e1600891.

563 Frieling, J., Peterse, F., Lunt, D. J., Bohaty, S. M., Sinninghe Damsté, J. S., Reichart, G. J., & Sluijs,  
564 A. (2019). Widespread Warming Before and Elevated Barium Burial During the Paleocene–  
565 Eocene Thermal Maximum: Evidence for Methane Hydrate Release?. *Paleoceanography and*  
566 *Paleoclimatology*, 34(4), 546-566.

567 Gutjahr, M., Ridgwell, A., Sexton, P. F., Anagnostou, E., Pearson, P. N., Pälike, H., ... & Foster,  
568 G. L. (2017). Very large release of mostly volcanic carbon during the Palaeocene–Eocene  
569 Thermal Maximum. *Nature*, 548(7669), 573-577.

570 Heilmann-Clausen, C., Nielsen, O. B., & Gersner, F. (1985). Lithostratigraphy and depositional  
571 environments in the Upper Paleocene and Eocene of Denmark. *Bulletin of the Geological*  
572 *Society of Denmark*, 33, 287-323.

573 Hollis, C. J., Dunkley Jones, T., & Wade, B. S. (2019). The DeepMIP contribution to PMIP4:  
574 methodologies for selection, compilation and analysis of latest Paleocene and early Eocene  
575 climate proxy data, incorporating version 0.1 of the DeepMIP database. *Geoscientific Model*  
576 *Development Discussions*.

577 Hopmans, E. C., Weijers, J. W., Schefuß, E., Herfort, L., Damsté, J. S. S., & Schouten, S. (2004).  
578 A novel proxy for terrestrial organic matter in sediments based on branched and isoprenoid  
579 tetraether lipids. *Earth and Planetary Science Letters*, 224(1-2), 107-116.

580 Hopmans, E. C., Schouten, S., & Damsté, J. S. S. (2016). The effect of improved chromatography  
581 on GDGT-based palaeoproxies. *Organic Geochemistry*, 93, 1-6.

582 Inglis, G. N., Farnsworth, A., Collinson, M. E., Carmichael, M. J., Naafs, B. D. A., Lunt, D. J., ... &  
583 Pancost, R. D. (2019). Terrestrial environmental change across the onset of the PETM and the  
584 associated impact on biomarker proxies: A cautionary tale. *Global and Planetary Change*, 181,  
585 102991.

586 Inglis, G. N., Bragg, F., Burls, N., Evans, D., Foster, G. L., Huber, M., Lunt, D. J., Siler, N., Steinig,  
587 S., Wilkinson, R., Anagnostou, E., Cramwinckel, M., Hollis, C. J., Pancost, R. D., & Tierney, J. E.

588 (in review, 2020). Global mean surface temperature and climate sensitivity of the EECO, PETM  
589 and latest Paleocene, *Climate of the Past Discussions*, <https://doi.org/10.5194/cp-2019-167>

590 John, C. M., Bohaty, S. M., Zachos, J. C., Sluijs, A., Gibbs, S., Brinkhuis, H., & Bralower, T. J.  
591 (2008). North American continental margin records of the Paleocene-Eocene thermal  
592 maximum: Implications for global carbon and hydrological cycling. *Paleoceanography*, 23(2).

593 Jolley, D.W. & Widdowson, M. (2005). Did Paleogene North Atlantic rift-related eruptions  
594 drive early Eocene climate cooling? *Lithos*, 79, 355-366.

595 Jones, M. T., Jerram, D. A., Svensen, H. H. & Grove, C. (2016). The effects of large igneous  
596 provinces on the global carbon and sulphur cycles. *Palaeogeography Palaeoclimatology*  
597 *Palaeoecology*, 441, 4-21.

598 Jones, M. T., Percival, L. M., Stokke, E. W., Frieling, J., Mather, T. A., Riber, L., ... & Svensen, H.  
599 H. (2019). Mercury anomalies across the Palaeocene–Eocene thermal maximum. *Climate of*  
600 *the Past*, 15(1).

601 Kender, S., Stephenson, M. H., Riding, J. B., Leng, M. J., Knox, R. W. B., Peck, V. L., ... &  
602 Jamieson, R. (2012). Marine and terrestrial environmental changes in NW Europe preceding  
603 carbon release at the Paleocene–Eocene transition. *Earth and Planetary Science Letters*, 353,  
604 108-120.

605 Kim, J. H., Van der Meer, J., Schouten, S., Helmke, P., Willmott, V., Sangiorgi, F., ... & Damsté,  
606 J. S. S. (2010). New indices and calibrations derived from the distribution of crenarchaeal  
607 isoprenoid tetraether lipids: Implications for past sea surface temperature reconstructions.  
608 *Geochimica et Cosmochimica Acta*, 74(16), 4639-4654.

609 King C. (2016). *A Revised Correlation of Tertiary Rocks in the British Isles and Adjacent Areas*  
610 *of NW Europe* (Gale, A.S. & Barry, T.L., editors). Special reports, 27. The Geological Society,  
611 London.

612 Knox, R.W.O'B., Bosch, J.H.A., Rasmussen, E.S., Heilmann-Clausen, C., Hiss, M., De Lugt, I.R.,  
613 Kasinski, J., King, C., Köthe, A., Slodkowska, B., Standke, G., Vandenberghe, N. (2010).  
614 Cenozoic. In: Dornenbaal, H., Stevenson, A. (Eds.), *Petroleum Geological Atlas of the Southern*  
615 *Permian Basin Area*. EAGE Publications b.v, Houten, pp. 211–223.

616 Larsen, R. B., & Tegner, C. (2006). Pressure conditions for the solidification of the Skaergaard  
617 intrusion: eruption of East Greenland flood basalts in less than 300,000 years. *Lithos*, 92(1-2),  
618 181-197.

619 Larsen, L. M., Fitton, J. G., & Pedersen, A. K. (2003). Paleogene volcanic ash layers in the Danish  
620 Basin: compositions and source areas in the North Atlantic Igneous Province. *Lithos*, 71(1), 47-  
621 80.

622 Littler, K., Röhl, U., Westerhold, T., & Zachos, J.C. (2014). A high-resolution benthic stable-  
623 isotope record for the South Atlantic: Implications for orbital-scale changes in Late Paleocene–  
624 Early Eocene climate and carbon cycling. *Earth and Planetary Science Letters*, 401, 18-30.

625 Ma, Z., Gray, E., Thomas, E., Murphy, B., Zachos, J., & Paytan, A. (2014). Carbon sequestration  
626 during the Palaeocene–Eocene Thermal Maximum by an efficient biological pump. *Nature*  
627 *Geoscience*, 7(5), 382-388.

628 McInerney, F. A., & Wing, S. L. (2011). The Paleocene-Eocene Thermal Maximum: A  
629 perturbation of carbon cycle, climate, and biosphere with implications for the future. *Annual*  
630 *Review of Earth and Planetary Sciences*, 39, 489-516.

631 Ogg, J., (2012). Geomagnetic Polarity Time Scale, in: Gradstein, F., Ogg, J., Schmitz, M., Ogg,  
632 G. (Eds.), *The Geologic Time Scale 2012*. Elsevier, pp. 85-113.

633 Peters, K. E., Peters, K. E., Walters, C. C., & Moldowan, J. M. (2005). *The biomarker guide* (Vol.  
634 1). Cambridge University Press.

635 Peterse, F., Kim, J. H., Schouten, S., Kristensen, D. K., Koç, N., & Damsté, J. S. S. (2009).  
636 Constraints on the application of the MBT/CBT palaeothermometer at high latitude  
637 environments (Svalbard, Norway). *Organic Geochemistry*, 40(6), 692-699.

638 Robock, A., (2000). Volcanic eruptions and climate. *Reviews of Geophysics*, 38, 191-219.

639 Schaller, M. F., Fung, M. K., Wright, J. D., Katz, M. E., & Kent, D. V. (2016). Impact ejecta at the  
640 Paleocene-Eocene boundary. *Science*, 354(6309), 225-229.

641 Schmidt, A., Skeffington, R.A., Thordarson, T., Self, S., Forster, P.M., Rap, A., Ridgwell, A.,  
642 Fowler, D., Wilson, M., Mann, G.W., Wignall, Paul B., & Carslaw, K.S. (2016). Selective  
643 environmental stress from sulphur emitted by continental flood basalt eruptions. *Nature*  
644 *Geoscience*, 9, 77-82.

645 Schmitz, B., Peucker-Ehrenbrink, B., Heilmann-Clausen, C., Åberg, G., Asaro, F., & Lee, C. T. A.  
646 (2004). Basaltic explosive volcanism, but no comet impact, at the Paleocene–Eocene  
647 boundary: high-resolution chemical and isotopic records from Egypt, Spain and Denmark.  
648 *Earth and Planetary Science Letters*, 225(1-2), 1-17.

649 Schoon, P. L., Heilmann-Clausen, C., Schultz, B. P., Damsté, J. S. S., & Schouten, S. (2015).  
650 Warming and environmental changes in the eastern North Sea Basin during the Palaeocene–  
651 Eocene Thermal Maximum as revealed by biomarker lipids. *Organic geochemistry*, 78, 79-88.

652 Schouten, S., Hopmans, E. C., Schefuß, E., & Damste, J. S. S. (2002). Distributional variations in  
653 marine crenarchaeotal membrane lipids: a new tool for reconstructing ancient sea water  
654 temperatures?. *Earth and Planetary Science Letters*, 204(1-2), 265-274.

655 Sluijs, A., Schouten, S., Pagani, M., Woltering, M., Brinkhuis, H., Damsté, J. S. S., ... &  
656 Matthiessen, J. (2006). Subtropical Arctic Ocean temperatures during the Palaeocene/Eocene  
657 thermal maximum. *Nature*, 441(7093), 610.

658 Sluijs, A., Bijl, P. K., Schouten, S., Röhl, U., Reichert, G. J., & Brinkhuis, H. (2011). Southern  
659 ocean warming, sea level and hydrological change during the Paleocene-Eocene thermal  
660 maximum. *Climate of the Past*, 7(1), 47-61.

661 Storey, M., Duncan, R. A., & Swisher, C. C. (2007a). Paleocene-Eocene thermal maximum and  
662 the opening of the northeast Atlantic. *Science*, 316 (5824), 587-589.

663 Storey, M., Duncan, R.A. & Tegner, C. (2007b). Timing and duration of volcanism in the North  
664 Atlantic Igneous Province: Implications for geodynamics and links to the Iceland hotspot.  
665 *Chemical Geology*, 241(3): 264-281.

666 Svensen, H., Planke, S., Malthes-Sørensen, A., Jamtveit, B., Myklebust, R., Eidem, T. R., & Rey,  
667 S. S. (2004). Release of methane from a volcanic basin as a mechanism for initial Eocene global  
668 warming. *Nature*, 429(6991), 542.

669 Thordarson, T., & Self, S. (2003). Atmospheric and environmental effects of the 1783–1784  
670 Laki eruption: A review and reassessment. *Journal of Geophysical Research: Atmospheres*,  
671 108(D1), AAC-7.

672 Tierney, J. E., & Tingley, M. P. (2014). A Bayesian, spatially-varying calibration model for the  
673 TEX86 proxy. *Geochimica et Cosmochimica Acta*, 127, 83-106.

674 van der Meulen, B., Gingerich, P. D., Lourens, L. J., Meijer, N., van Broekhuizen, S., van  
675 Ginneken, S., & Abels, H. A. (2020). Carbon isotope and mammal recovery from extreme  
676 greenhouse warming at the Paleocene–Eocene boundary in astronomically-calibrated fluvial  
677 strata, Bighorn Basin, Wyoming, USA. *Earth and Planetary Science Letters*, 534, 116044.

678 Weijers, J. W., Schouten, S., Spaargaren, O. C., & Sinninghe Damsté, J. S. (2006). Occurrence  
679 and distribution of Tetraether membrane lipids in soils: Implications for the use of the TEX86  
680 proxy and the BIT index, *Organic Geochemistry*, 37, 10 1680-1693.

681 Westerhold, T., Röhl, U., McCarren, H. K., & Zachos, J. C. (2009). Latest on the absolute age of  
682 the Paleocene–Eocene Thermal Maximum (PETM): new insights from exact stratigraphic  
683 position of key ash layers+ 19 and– 17. *Earth and Planetary Science Letters*, 287(3-4), 412-419.

684 Westerhold, T., Röhl, U., Wilkens, R. H., Gingerich, P. D., Clyde, W. C., Wing, S. L., Bowen, G. J.,  
685 and Kraus, M. J. (2018). Synchronizing early Eocene deep-sea and continental records –  
686 cyclostratigraphic age models for the Bighorn Basin Coring Project drill cores, *Clim. Past*, 14,  
687 303-319.

688 Wieczorek, R., Fantle, M.S., Kump, L.R., & Ravizza, G. (2013). Geochemical evidence for  
689 volcanic activity prior to and enhanced terrestrial weathering during the Paleocene Eocene  
690 Thermal Maximum. *Geochimica et Cosmochimica Acta*, 119, 391-410.

691 Zachos, J. C., Schouten, S., Bohaty, S., Quattlebaum, T., Sluijs, A., Brinkhuis, H., ... & Bralower,  
692 T. J. (2006). Extreme warming of mid-latitude coastal ocean during the Paleocene-Eocene  
693 Thermal Maximum: Inferences from TEX86 and isotope data. *Geology*, 34(9), 737-740.

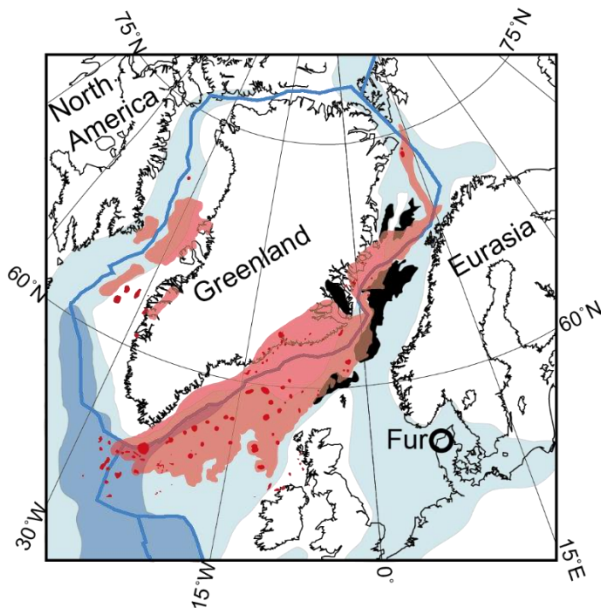
694 Zachos, J. C., McCarren, H., Murphy, B., Röhl, U., & Westerhold, T. (2010). Tempo and scale  
695 of late Paleocene and early Eocene carbon isotope cycles: Implications for the origin of  
696 hyperthermals. *Earth and Planetary Science Letters*, 299(1-2), 242-249.

697 Zeebe, R. E., & Lourens, L. J. (2019). Solar System chaos and the Paleocene–Eocene boundary  
698 age constrained by geology and astronomy. *Science*, 365(6456), 926-929.

699 Zhang, Y. G., Zhang, C. L., Liu, X. L., Li, L., Hinrichs, K. U., & Noakes, J. E. (2011). Methane Index:  
700 a tetraether archaeal lipid biomarker indicator for detecting the instability of marine gas  
701 hydrates. *Earth and Planetary Science Letters*, 307(3-4), 525-534.

702 Zhang, Y. G., Pagani, M., & Wang, Z. (2016). Ring Index: A new strategy to evaluate the integrity  
703 of TEX86 paleothermometry. *Paleoceanography*, 31(2), 220-232.

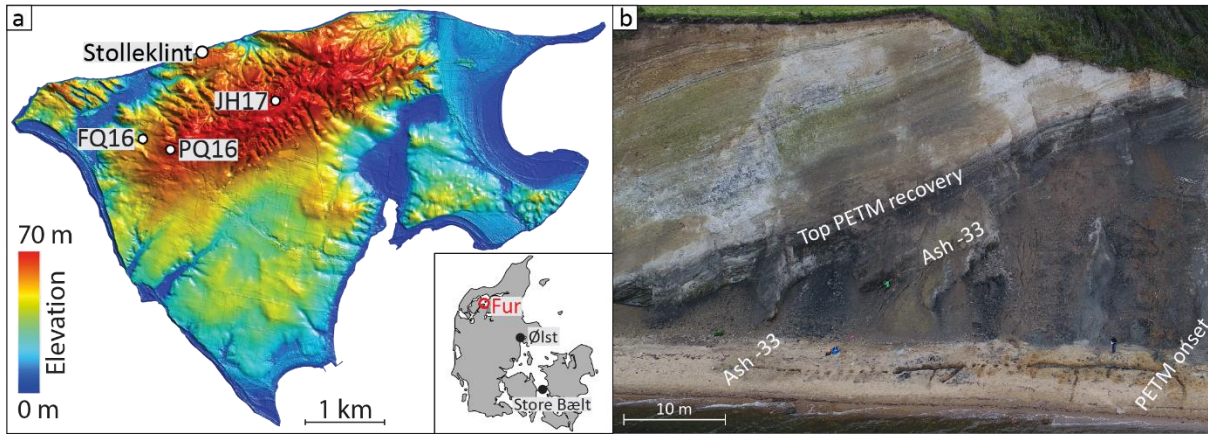
#### 704 Figures



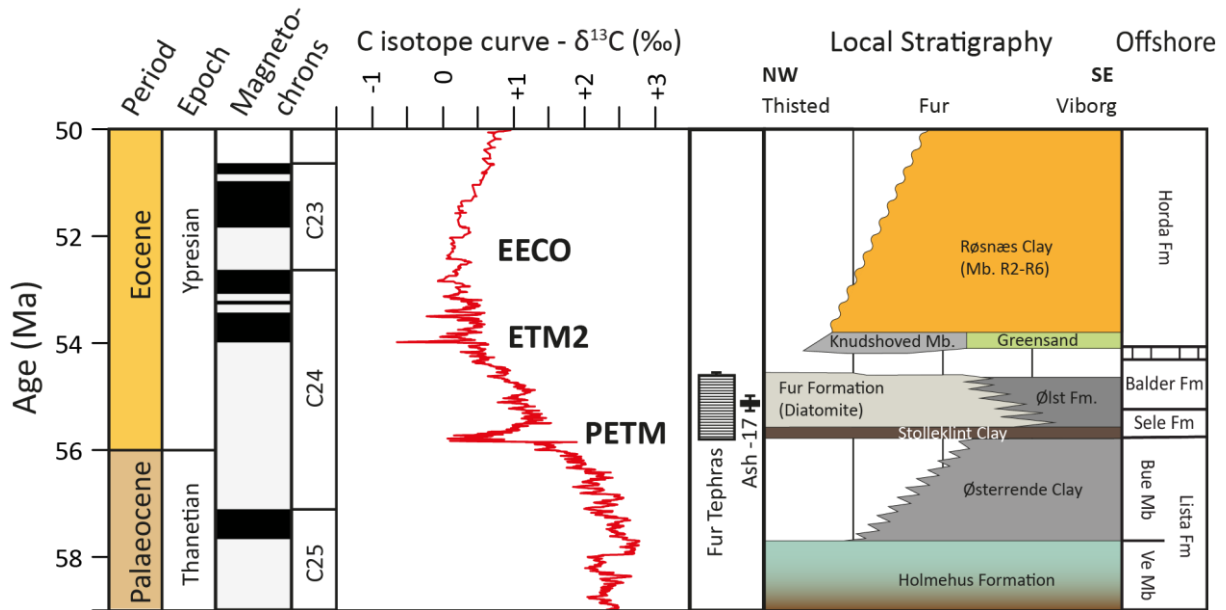
705  
706 **Figure 1:** Location of the island of Fur in a plate reconstruction at 56 Ma with the known extent of the NAIP  
707 indicated. Blue lines: plate boundaries. Black lines: present day coastlines. Light and dark blue areas: shelf and  
708 deep marine areas respectively. Light red areas: Known extent of subaerial and submarine volcanism from the



709 NAIP. Dark red: individual volcanic centres. Black areas: extent of known NAIP sill intrusions in sedimentary  
 710 basins. Figure modified from Jones et al. (2019).

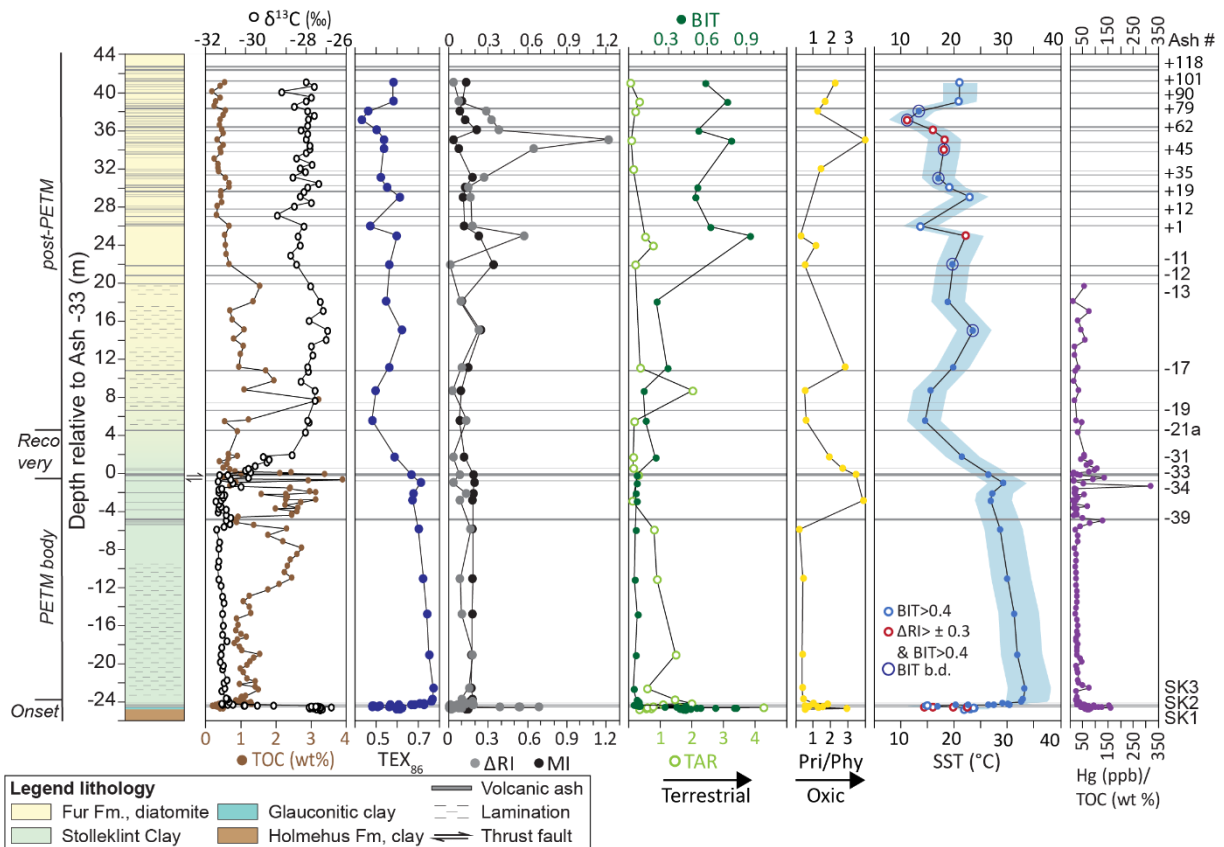


711  
 712 **Figure 2:** a) Topographic map of the island of Fur. Samples are from four marked localities: the main locality  
 713 Stolleklint (56°50'29"N, 8°59'33"E), the quarries near Fur Camping (FQ16 at 56°49'51"N, 8°58'45"E and PQ16  
 714 at 56°49'48"N 8°59'07"E), and Jenshøy (JH17; 56°50'05"N 9°00'31"E). The high topography in the north of the  
 715 island is a partially overturned anticline of Fur Fm. and upper Stolleklint Clay strata. Map courtesy of Egon  
 716 Nørmark. b) Photo of the Stolleklint beach from the sea, with the PETM indicated. The boundary between the  
 717 Stolleklint Clay and Fur Fm. is at Ash -33, followed by a gradual transition from clay to diatomite. The inclined  
 718 bedding is due to the glaciotectionic folding. Note the 43 m long trench along the beach.

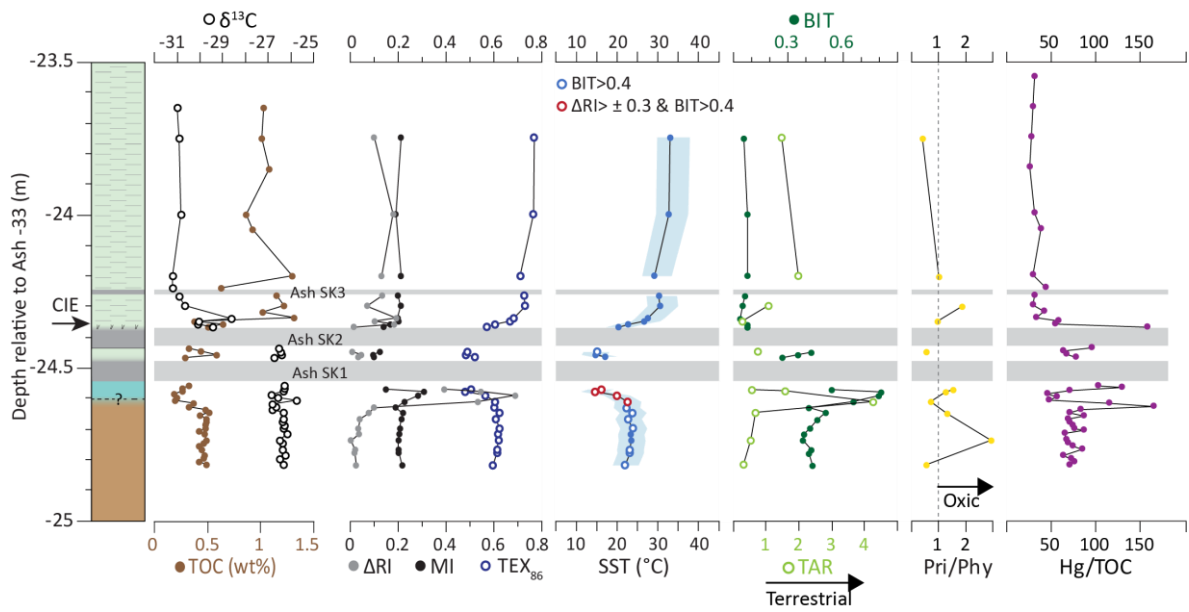


719

720 **Figure 3:** Composite figure of the Paleocene-Eocene interval, indicating both the local Danish stratigraphy and  
 721 the correlative offshore North Sea stratigraphy in relation to the PETM and other intervals of environmental  
 722 change during the Palaeogene. Local stratigraphic section courtesy of Claus Heilmann-Clausen, offshore  
 723 correlation adapted from King (2016). Carbon isotope data from Cramer et al. (2009) and Littler et al. (2014) and  
 724 plotted on the GTS2012 timescale (Ogg, 2012). PETM = Paleocene-Eocene Thermal Maximum; ETM2 = Eocene  
 725 Thermal Maximum 2; EECO = Early Eocene Climatic Optimum.

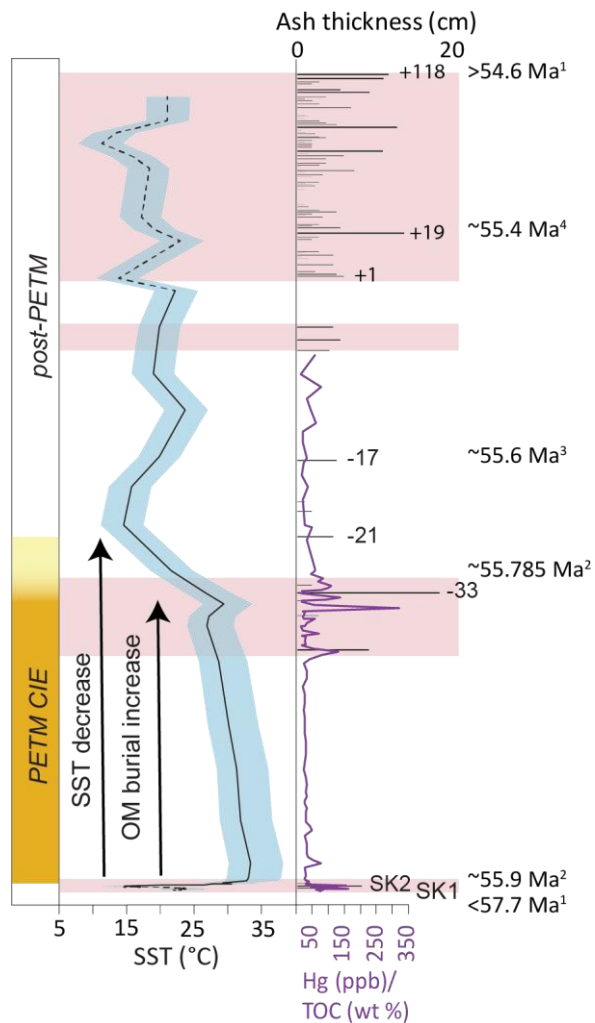


726 **Figure 4:** Composite data from the island of Fur, combining samples from Stolleklint beach and three nearby  
 727 quarries. Data includes  $\delta^{13}\text{C}$  and TOC analyses,  $\text{TEX}_{86}$  values, BAYSPAR calibrated  $\text{TEX}_{86}$  SSTs with  $1\sigma$  errorbars  
 728 indicated by blue area, several organic biomarker ratios, and mercury/TOC from Jones et al. (2019). Hg values  
 729 are included in the Supplementary data. Composite log of the local lithology and its relation to the interpreted  
 730 PETM-onset, -body and -recovery, and post-PETM sections shown on the left. Grey lines indicate ash layers, with  
 731 the ash stratigraphy indicated on the right. Legend shown at the base. TOC = Total Organic Carbon; SST = Sea  
 732 Surface Temperature;  $\Delta\text{RI}$  = Ring Index; MI = Methane Index; BIT = Branched and Isoprenoid Tetraether index;  
 733 TAR = Terrigenous Aquatic Ratio; Pri/Phy = Pristane/Phytane.



735

736 **Figure 5:** Zoom-in of Figure 4 showing data covering the PETM onset at Fur. Samples from the base of Stolleklint  
 737 beach. Data include  $\delta^{13}\text{C}$  and TOC analyses,  $\text{TEX}_{86}$  values, BAYSPAR calibrated  $\text{TEX}_{86}$  SSTs with  $1\sigma$  errorbars  
 738 indicated by blue area, several organic biomarker ratios, and mercury/TOC from Jones et al. (2019). Composite  
 739 log of the local lithology and its relation to the interpreted PETM-onset shown on the left. Grey bands indicate  
 740 ash layers SK1, SK2, and SK3. Legend shown in Fig. 4. TOC = Total Organic Carbon; SST = Sea Surface Temperature;  
 741  $\Delta\text{RI}$  = Ring Index; MI = Methane Index; BIT = Branched and Isoprenoid Tetraether index; TAR = Terrigenous  
 742 Aquatic Ratio; Pri/Phy = Pristane/Phytane.



743

744 **Figure 6:** Summary of temperature changes and volcanic proxies. Red bands show periods of active NAIP  
 745 volcanism as indicated by high ash accumulation and Hg/TOC anomalies. Yellow band indicate duration of the  
 746 PETM carbon isotope excursion (CIE). Black line show BAYSPAR calibrated Sea Surface Temperatures (SST), where  
 747 blue band indicate the associated  $1\sigma$  error, and dashed line SSTs with high potential  $TEX_{86}$  bias. OM=Organic  
 748 Matter; TOC=Total Organic Carbon; <sup>1</sup>King (2016); <sup>2</sup>Charles et al. (2011), assuming the timings of the Svalbard and  
 749 Fur CIEs are coeval; <sup>3</sup>Storey et al. (2007a); <sup>4</sup>Westerhold et al. (2009).